A Mg isotopic perspective on the mobility of magnesium during serpentinization and carbonation of the Oman ophiolite

Juan Carlos de Obeso[1*], Danielle P. Santiago Ramos[2^], John A. Higgins[2], Peter B. Kelemen[3]

[1] Lamont Doherty Earth Observatory, Columbia University, Palisades, NY, USA

[2] Department of Geosciences, Princeton University, Princeton, NJ, USA

[3] Dept. of Earth & Environmental Sciences, Columbia University, Lamont Doherty Earth Observatory,

Palisades, NY, USA

[^] now at Geology & Geophysics, Woods Hole Oceanographic Institution, Wood Hole, MA, USA

*Corresponding author: Juan Carlos de Obeso ([deobeso@ldeo.columbia.edu,](deobeso@ldeo.columbia.edu) [jcdeobeso@gmail.com)](jcdeobeso@gmail.com) Orcid: 0002-9962-8177

Key Points:

- The range of $\delta^{26}Mg$ from samples of the mantle section in the Oman ophiolite is ~4.5‰, or >60% of the total range of terrestrial variability.
- The range in $\delta^{26}Mg$ values involves co-precipitation of serpentine and carbonates at high water-to-rock ratios.
- Serpentinization and carbonation is ongoing in the mantle section of the Oman ophiolite.

(The above elements should be on a title page)

1 **Abstract**

2   Alteration of mantle peridotite in the Samail ophiolite forms secondary minerals, mainly

3 serpentine and Mg-rich carbonates. Magnesium accounts for approximately 25 to 30% of

4 peridotite mass and its mobility can be used to trace this alteration. We report the first set of Mg

5 isotope measurements from peridotites and their alteration products in Oman. Partially

6 serpentinized peridotites have Mg isotope ratios that are indistinguishable from estimates for the

7 average mantle and bulk silicate earth ($\delta^{26}Mg$ =-0.25±0.04‰). However, more extensively altered

8 peridotite samples show large shifts in Mg isotopic composition. The range of $\delta^{26}Mg$ values for

9 our suite of alteration products from the mantle section is ~4.5‰, or >60% of the total range of

10 terrestrial variability in $\delta^{26}Mg$ values. Serpentine veins are typically enriched in ^{26}Mg (up to

11 0.96‰) whereas Mg-carbonate veins are associated with low $^{26}Mg/^{24}Mg$ ratios (magnesite $\delta^{26}Mg$

12 =-3.3‰, dolomite $\delta^{26}Mg$ =-1.91‰). Our preferred explanation for the range in $\delta^{26}Mg$ values

13 involves co-precipitation of serpentine and carbonates at water-to-rock ratios $>10^3$. The

14 coincidence of alteration products characterized by $\delta^{26}Mg$ values that are both lower and higher

15 than bulk silicate Earth and the finite ^{14}C ages of the carbonates suggest that both serpentinization

16 and carbonation are ongoing in Oman. Rates of calcite precipitation in travertines inferred from

17 $\Delta^{26}Mg_{cal-fl}$ suggest that travertine formation in Oman sequesters a total of 10^6-10^7 kg CO_2/yr,

18 consistent with previous estimates.

19

20 **1. Introduction**
21
22
23   Alteration of ultramafic rocks is ubiquitous in near-surface environments, both on land and

24 below the seafloor. Mantle olivine and pyroxene are unstable at near-surface conditions and

25 undergo hydration (serpentinization) and carbonation when fluids are present (e.g. Moody, 1976).

26 These reactions result in the formation of serpentine minerals, carbonates, brucite, magnetite and

27 other Fe-oxides and hydroxides. Serpentinization and carbonation reactions are often nearly

28 isochemical apart from the addition of H_2O and CO_2 (e.g., Coleman & Keith 1971). Both

29 observations and thermodynamic modeling suggest that changes in major element ratios such as

30 Si/Mg are minor (e.g. $\leq 10\%$ for low temperature reaction with seawater, Malvoisin, 2015, Figure

31 3; Monnier et al., 2006; Snow and Dick, 1995). However, other studies (e.g. Al-Khirbash, 2015;

32 Auclair et al., 1993; Beinlich et al., 2018; de Obeso and Kelemen, 2018; Esteban Guzman et al.,

33 2011; Hotz, 1964; Nasir et al., 2007; Skarpelis, 2006, de Obeso and Kelemen, 2020) have shown

34 that under certain conditions mass transfer during serpentinization can lead to larger changes in

35 major element chemistry. In Oman, while partially serpentinized harzburgites record a $\sim 2\%$

36 decrease in MgO/SiO_2 compared to the inferred composition of unaltered mantle peridotites

37 (Monnier et al., 2006), there are examples of heavily altered harzburgite that have lost up to 30%

38 of their original Mg (de Obeso and Kelemen, 2020).

39

40   Magnesium isotope studies show that the composition of the mantle and bulk silicate earth

41 (BSE) is relatively uniform, with $\delta^{26}Mg$ values= -0.25±0.04‰ (2σ), (Teng, 2017; Teng et al.,

42 2010). Liu et al. (2017) report $\delta^{26}Mg$ values of -0.12±0.13 ‰ (2σ) for altered seafloor peridotites.

43 There are a limited number of studies on magnesium isotope compositions of ophiolite peridotites.

44 Peridotites from the Purang ophiolite (Tibet) have $\delta^{26}Mg$=-0.20±0.10‰ (2σ), within uncertainty

45 of mantle compositions (Su et al., 2015), while peridotites from the Feragen and Linnajavri

46 ultramafic bodies (Norway) have mantle-like Mg isotope ratios, with $\delta^{26}Mg$ values ranging from

47 −0.35‰ to −0.23‰ (Beinlich et al., 2014).

48

49   Magnesium isotopes are known to fractionate during precipitation of carbonates and

50   silicates from aqueous fluids. This fractionation can be used to constrain alteration processes

51   during serpentinization and carbonation. Carbonates preferentially incorporate ^{24}Mg during

52   crystallization, as observed in both experimental and natural samples, which yield large

53   fractionation factors (Higgins and Schrag, 2010; Li et al., 2015; Mavromatis et al., 2013; Pearce

54   et al., 2012; Shirokova et al., 2013; Tipper et al., 2006). On the other hand, available constraints

55   on Mg fractionation factors associated with formation of serpentine polymorphs are equivocal. For

56   example, based on dissolution experiments of San Carlos olivine at low temperature (~25°C),

57   Wimpenny et al., (2010) suggested that chrysotile preferentially removed light Mg from solution.

58   In contrast, Ryu et al. (2016) synthetized lizardite from solution and reported that the mineral

59   product was enriched in heavy Mg relative to the fluid at experimental temperatures of 90 and

60   250°C. Following a molecular dynamics approach, Wang et al. (2019) also concluded that lizardite

61   crystallization preferentially removes ^{26}Mg from the fluid. These experimental results contrast

62   with fractionation estimates based on natural samples that concluded that serpentinization does not

63   fractionate Mg isotopes (Beinlich et al., 2014; Liu et al., 2017; Oskierski et al., 2019). Studies of

64   natural samples also suggest that talc and Mg-rich clays formed during alteration are enriched in

65   ^{26}Mg (Beinlich et al., 2014; Liu et al., 2017). In summary, whereas carbonate/water fractionation

66   factors are large, those for serpentine are uncertain but close to 1. Thus Mg isotopes should be

67   sensitive to the conditions of serpentinization and carbonation. Under closed system or low-water-

68   to-rock conditions we expect little variability in Mg isotopes but at high water-to-rock ratios the

69   full Mg isotope fractionation between Mg carbonate and silicates can be expressed.

70

71   To explore the behavior of Mg and Mg isotopes during serpentinization and carbonation we

72   present the first suite of Mg isotope analyses of bulk-rock samples and mineral separates from the

73   Samail ophiolite in Oman. Our sample suite consists of 37 samples of harzburgites and dunites

74   with different degrees of alteration, as well as products of peridotite alteration (silicates and

75   carbonates). We find that while the Mg isotopic compositions of partially serpentinized Oman

76   peridotites (average $\delta^{26}Mg$= -0.25±0.14‰, 2σ) are indistinguishable from mantle values,

77   serpentine and carbonate samples are ^{26}Mg-enriched (up to 0.96‰) and ^{26}Mg-depleted (up to -

78   3.38‰), respectively, compared to average mantle. We explore different hypotheses to explain the

79   co-occurrence of high $\delta^{26}Mg$ serpentines and low $\delta^{26}Mg$ carbonates and discuss results in the

80   context of previously published ^{14}C analyses which indicate that serpentinization and carbonation

81   are ongoing during weathering of the Samail ophiolite mantle section.

82

83   **2. Geological background and sample selection**

84   The Samail ophiolite in eastern Oman is the best-exposed section of oceanic crust and

85   mantle in the world (Figure 1). The mantle section of the ophiolite is composed of highly depleted

86   harzburgites together with ~5-15% dunite (Boudier and Coleman, 1981; Braun, 2004; Braun and

87   Kelemen, 2002; Collier, 2012). These peridotites exhibit different degrees of alteration ranging

88   from ~30% serpentinized in "fresh" rocks to instances of completely serpentinized (Godard et al.,

89   2000; Monnier et al., 2006) and completely carbonated peridotites (Falk and Kelemen, 2015; Nasir

90   et al., 2007; Stanger, 1985). There is substantial evidence that alteration occurred throughout the

91   history of the ophiolite. $\delta^{18}O$ data suggest that some alteration occurred near the axis of the

92   spreading center as seawater interacted with the Samail crust (Gregory and Taylor, 1981), while

93   an internal $^{87}Sr/^{86}Sr$ isochron on listvenite (carbonated peridotite) shows that alteration continued

94   during obduction and emplacement (Falk and Kelemen, 2015). The presence of hyperalkaline

95   springs, recently crystallized carbonate veins and highly reduced fluids and mineral assemblages

96   indicates that alteration is ongoing (e.g. Chavagnac et al., 2013a, 2013b; Clark and Fontes, 1990;

97   Coleman and Keith, 1971; Kelemen et al., 2011; Kelemen and Matter, 2008; Mervine et al., 2014;

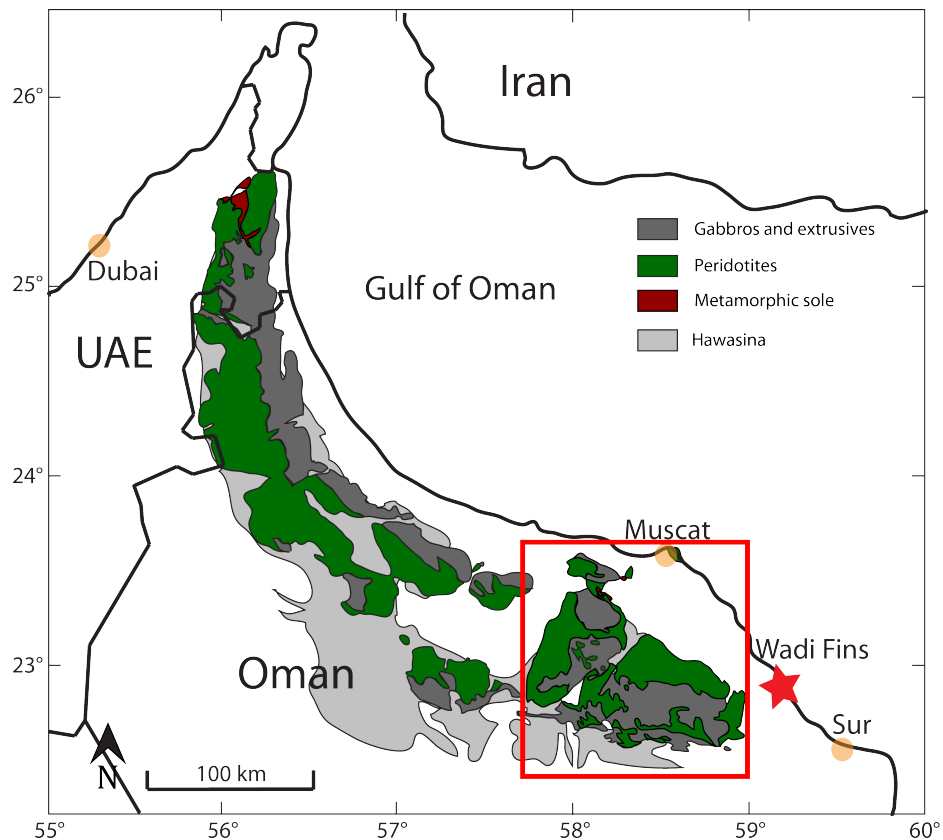98   Monnin et al., 2011; Neal and Stanger, 1985; Streit et al., 2012).

99

100
101   **Figure 1.** Simplified geologic map of the Samail ophiolite in Oman and the United Arab
102   Emirates. All samples in this study come from the southern massifs (red square) and a small
103   exposure beneath overlying Cretaceous to Eocene limestones at Wadi Fins (red star). Modified
104   after (Nicolas et al., 2009).

105

106   Previous studies of low-temperature alteration of the Oman ophiolite propose that it occurs

107   in three steps (e.g. Barnes et al., 1978, 1967; Barnes and O'Neil, 1969; Chavagnac et al., 2013a;

108   Kelemen et al., 2011; Neal and Stanger, 1985; Noël et al., 2018; Paukert et al., 2012). Step 1 is

109   characterized by formation of Mg^{2+}-HCO_3^- rich fluids, as rain water dissolves Mg from peridotite

110   and CO_2 from the atmosphere during near-surface weathering. During step 2, this so-called "Type

111   I" water percolates deeper into peridotite leading to precipitation of Mg-rich carbonates, brucite

112   and serpentine. These reactions remove carbon and Mg^{2+} from the fluid and dissolve Ca^{2+}, which

113   is incompatible in the alteration minerals. The resulting fluids, known as "Type II" waters, have

114   low Mg and C, high Ca and pH, and very low oxygen fugacities (Bruni et al., 2002; Clark and

115   Fontes, 1990; Neal and Stanger, 1983; Paukert et al., 2012). During step 3, hyperalkaline "Type

116   II" fluids are returned to the surface, where disequilibrium with the atmosphere leads to rapid

117   uptake of atmospheric CO_2 and precipitation of calcite to form travertine deposits (Chavagnac et

118   al., 2013a; Clark and Fontes, 1990; Kelemen et al., 2011; Kelemen and Matter, 2008; Mervine et

119   al., 2014; Neal and Stanger, 1985; Paukert et al., 2012).

120

121   Magnesium fluxes during these three stages of alteration remain poorly constrained but

122   inferences of water/rock during alteration have been made for Oman peridotites. Sulfides and in

123   some cases native metals recording low oxygen fugacity observed in partially serpentinized

124   peridotites are associated with low water/ratios (W/R) and incipient serpentinization (de Obeso

125   and Kelemen, 2020; Frost, 1985; Kelemen et al., 2020; Lorand, 1988). Increased W/R are inferred

126   from changes in accessory sulfide minerals (de Obeso and Kelemen, 2020) and the occurrence of

127   diffuse carbonate vein networks in the peridotites (Noël et al., 2018). Even higher W/R are

128   expected to have been involved in the formation of massive carbonate-serpentine veins which

129   acted as main fluid paths for fluids interacting with peridotites (de Obeso and Kelemen, 2018;

130   Noël et al., 2018). Secondary minerals from the three steps formed at variable W/R have different

131   aqueous Mg^{2+}-mineral fractionation properties with silicates expected to become enriched in ^{26}Mg

132   and carbonates enriched in ^{24}Mg (e.g. Beinlich et al., 2014; Gao et al., 2018; Liu et al., 2017;

133   Pinilla et al., 2015; Wang et al., 2019; Wimpenny et al., 2014) suggesting that Mg isotopes can be

134   used as tracers of alteration.

135

136   All samples analyzed here were collected from the southern massifs of the ophiolite, within

137   its mantle section (Figure 1). Previously described samples analyzed for this study can be separated

138   into silicate- and carbonate-bearing groups. Silicate samples include relatively fresh harzburgites

139   (n=6, average ~ 40% relict mantle minerals) and dunites (n=4, ~23%) from Hanghøj et al. (2010),

140   highly serpentinized harzburgites (n=2, 37 and 14%) and dunites (n=1, 0%) from de Obeso and

141   Kelemen (2018), and a set of serpentinized harzburgites (n=3, ~40%), high-Si harzburgite (n=3,

142   0%) and oxidized harzburgite (n=3, 0%) from de Obeso and Kelemen, 2020. We also include four

143   samples not previously described: two serpentine veins, one serpentinite, and a "waxy vein" from

144   a serpentinized body with Mg/Si~1.

145

146   Carbonate samples include two groups: completely carbonated peridotites, also known as

147   listvenites, from Falk & Kelemen (2015), further classified as dolomite listvenites (n=2) and

148   magnesite listvenites (n=2). We also analyzed massive carbonate veins from serpentinized

149   peridotite outcrops, including two magnesite veins and one dolomite vein (Kelemen et al., 2011).

150   The three carbonate vein samples have ^{14}C contents corresponding to ages of 32ka, 37ka, and 40ka

151   (Kelemen et al., 2011). Two travertine samples from Kelemen et al. (2011) were also analyzed.

152   These travertines are composed mainly of calcite, with ^{14}C contents corresponding to ages of 1630

153   and 18,450 years. We also include two carbonate vein samples not previously described: a massive

154   magnesite vein and a huntite vein. Major element compositions and locations for the new samples

155   are reported in table S1.

156

157   **3. Methods**

158   Samples not previously described (4 silicates and 2 carbonates) were processed in Lamont

159   Doherty Earth Observatory (LDEO). Samples were chipped using a jaw crusher and powdered

160   using an alumina puck mill. Major element analyses and loss on ignition (LOI) were performed

161   using an Agilent 720 Axial ICP-OES calibrated with rock standards (Table S2) following

162   dissolution by lithium metaborate fusion and nitric acid.

163

164   For Mg isotopic analyses powders of all 37 samples and three USGS rock standards (BCR-

165   2, BHVO-2, BIR-1A) were digested using a HNO_3:HF (3:1) digestion procedure at LDEO. Sample

166   OM17-magnesite was processed in multiple digestion batches to check reproducibility (n=5). Once

167   digested, < 1 μg of Mg from each sample was purified from the silicate/carbonate matrix using a

168   Thermo Dionex 5000+ ion chromatography (IC) system at Princeton University. The procedure

169   for both carbonate and silicate minerals is described in more detail in Husson et al. (2015) and

170   Santiago Ramos et al. (2020)

171

172   Isotopic analyses were carried out at Princeton University on a Thermo Fisher Scientific

173   Neptune Plus MC-ICP-MS. Standard-sample-standard bracketing was used to correct for

174   instrumental mass fractionation (Galy et al., 2001) and values were normalized to an internal

175   standard (DSM-3). Magnesium isotope ratios are reported using delta notation. Long-term external

176   reproducibility is estimated by comparing Mg standard Cambridge-1 against DSM-3 standard.

177   Measured δ^{26}Mg values for Cambridge-1 yield an average of -2.59 ± 0.05‰ (2σ, n= 7),

178   indistinguishable from the published value of -2.62±0.03‰ (2σ) (Galy et al., 2003; Teng et al.,

179   2015). Reported uncertainties for each sample depend on the number of times the sample has been

180   separated and analyzed. For a single separation and analysis, we report the long-term external

181   reproducibility of Cambridge-1 (δ^{26}Mg $2\sigma=\pm0.09$‰). USGS standards ran as unknowns are

182   reported in Table S3. For multiple chromatographic separations and analyses (n> 1) we report the

183   standard error of the mean (SE). All analyzed samples fall on an isotopic mass-dependent

184   fractionation line in three-isotope space with slope of 0.5196±0.0024 (R^2=0.9992),

185   indistinguishable from the value of 0.5210 estimated for equilibrium fractionation (Young and

186   Galy, 2004). Given the linear relationship in three-isotope space, we discuss only δ^{26}Mg values.

187

188   **4. Results**

189   Measured δ^{26}Mg and δ^{25}Mg values for the sample suite are presented in Table 1 and shown

190   in Figure 2. The observed range for this study is ~4.6‰ (-3.4‰ to +1.2‰), or >60% of the

191   observed variability in δ^{26}Mg values on Earth (~7.5‰, from -5.6‰ to +1.8‰; Teng, 2017), and

192   include δ^{26}Mg values that are both higher than and lower than unaltered mantle peridotite.

193

194

195

196

197

198

199

Sample	Reference	Lithology	$\delta^{26}Mg$	$\delta^{25}Mg$	2σ/2SE	n
OM94-99	Hanghøj et al 2008	Dunite	-0.22	-0.11	0.09	1
OM94-52D*	Hanghøj et al 2008	Dunite	-0.25	-0.11	0.09	1
OM94-74D	Hanghøj et al 2008	Dunite	-0.32	-0.15	0.09	1
OM94-110*	Hanghøj et al 2008	Dunite	-0.17	-0.06	0.09	1
OM94-67	Hanghøj et al 2008	Harzburgite	-0.25	-0.12	0.09	1
OM94-103	Hanghøj et al 2008	Harzburgite	-0.22	-0.11	0.09	1
OM94-61	Hanghøj et al 2008	Harzburgite	-0.24	-0.09	0.09	1
OM94-98	Hanghøj et al 2008	Harzburgite	-0.20	-0.09	0.09	1
OM94-101	Hanghøj et al 2008	Harzburgite	-0.29	-0.16	0.09	1
OM94-52H	Hanghøj et al 2008	Harzburgite	-0.42	-0.22	0.09	1
OM13-19	De Obeso & Kelemen 2018	Harzburgite	-0.17	-0.09	0.09	1
OM13-2	De Obeso & Kelemen 2018	Harzburgite	-0.24	-0.14	0.09	1
OM13-4	De Obeso & Kelemen 2018	Dunite	-0.24	-0.09	0.09	1
OM15-5-4	De Obeso & Kelemen 2020	Harzburgite	-0.10	-0.07	0.09	1
OM15-6-4	De Obeso & Kelemen 2020	Harzburgite	-0.09	-0.03	0.09	1
OM15-7-4	De Obeso & Kelemen 2020	Harzburgite	-0.09	-0.07	0.09	1
OM15-5-3	De Obeso & Kelemen 2020	Oxidized harzburgite	0.94	0.49	0.09	1
OM15-6-3	De Obeso & Kelemen 2020	Oxidized harzburgite	0.86	0.46	0.09	1
OM15-7-3	De Obeso & Kelemen 2020	Oxidized harzburgite	0.77	0.41	0.09	1
OM15-6-2	De Obeso & Kelemen 2020	Altered harzburgite	0.74	0.38	0.09	1
OM15-7-2	De Obeso & Kelemen 2020	Altered harzburgite	0.74	0.40	0.09	1
OM15-5-2	De Obeso & Kelemen 2020	Altered harzburgite	0.70	0.37	0.09	1
OM13-15A	This Study	Serpentinite	0.17	0.08	0.09	1
OM15-5-5	This Study	Waxy vein	1.19	0.60	0.09	1
OM13-15B	This Study	Serpentine vein	0.45	0.20	0.09	1
OM13-17A WP	This Study	Serpentine vein	0.96	0.51	0.09	1
OM09-11	Falk and Kelemen 2015	Magnesite Listvenite	-0.33	-0.18	0.09	1
OM10-26	Falk and Kelemen 2015	Magnesite Listvenite	-0.33	-0.16	0.09	1
OM10-14	Falk and Kelemen 2015	Dolomite Listvenite	-1.46	-0.78	0.09	1
OM10-15	Falk and Kelemen 2015	Dolomite Listvenite	-0.89	-0.48	0.09	1
OM07-39	Streit et al. 2012	Massive magnesite vein	-3.14	-1.64	0.09	1
OM07-27	Streit et al. 2012	Massive dolomite vein	-1.91	-1.02	0.09	1
OM17 Magnesite	This study	Massive magnesite vein	-3.38	-1.77	0.01	5
OM07-18	Kelemen et al 2011	Travertine forming now	-1.14	-0.56	0.07	2
OM07-34A	Kelemen et al 2011	Old travertine	-0.89	-0.44	0.05	2
OM07-07	Kelemen et al 2011	Carbonate vein	-3.39	-1.75	0.09	1
BA1B 11-2 17-27 cm	This study from mineralogy	Huntite vein	-3.04	-1.57	0.09	1

2σ=long-term external reproducibility of Cambridge-1; applied to all samples that were run only once through column chemistry + Neptune (i.e. not replicated)
2SE=applied to samples that were replicated, that is, run through column chemistry + Neptune more than once

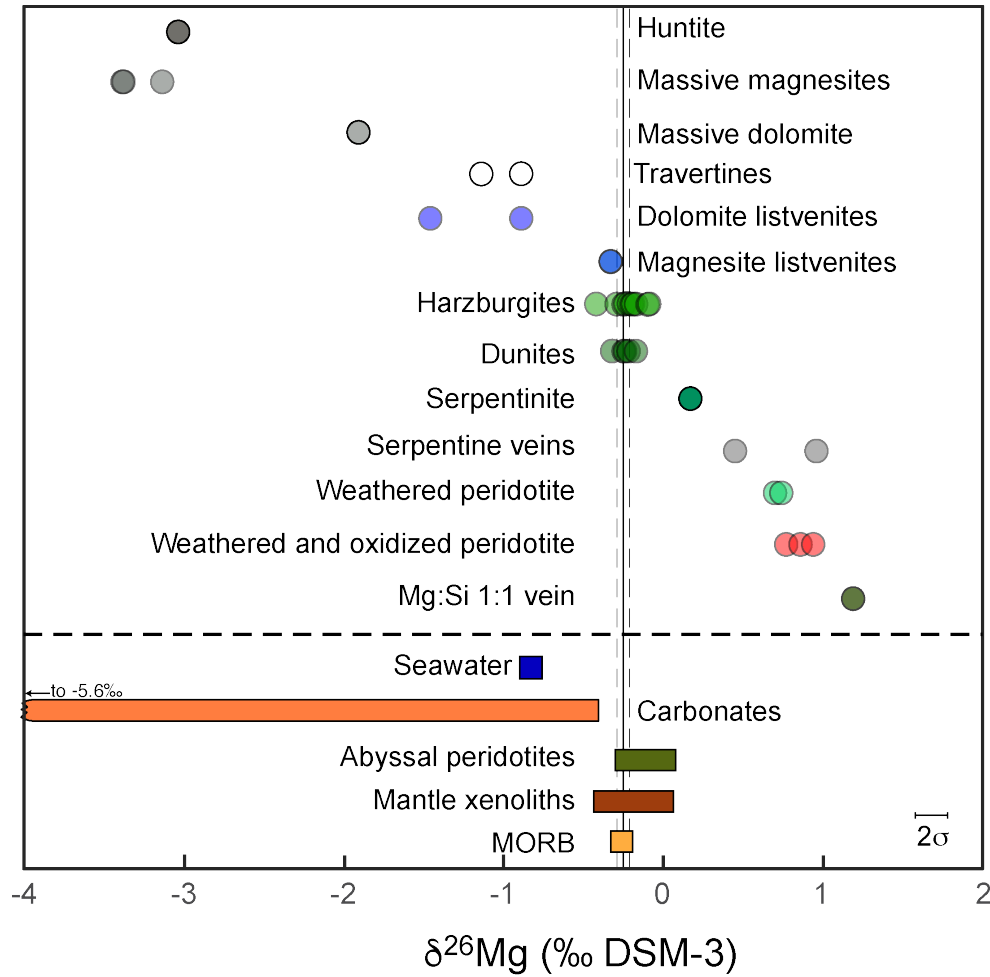200   **Table 1.** Samples numbers, reference, lithology and Mg isotopic compositions

Figure 2. δ^{26}Mg for studied samples from the Oman ophiolite and selected terrestrial reservoirs (colored rectangles from Teng 2017). Black solid line represents the average mantle value, and vertical dashed black lines delineate the range of variability of mantle compositions from Teng (2010, 2017). Earth δ^{26}Mg range is ~7.5‰ (Teng, 2017)

Measured δ^{26}Mg values in partially serpentinized harzburgites and dunites are indistinguishable from the mantle (-0.25±0.14‰ (2σ) and -0.24±0.10‰ (2σ), respectively, Figure 3). Three samples from Wadi Fins (OM15-5-4, OM15-6-4 and OM15-7-4; de Obeso and Kelemen, 2020) are characterized by average δ^{26}Mg values higher than the mantle (-0.09±0.01‰, 2σ) are excluded from the harzburgite average as their compositions record significant Mg leaching (up to 30% in the most altered samples). Their completely hydrated (OM15-5-2, OM15-6-2 and OM15-7-2) and oxidized (OM15-5-3, OM15-6-3 and OM15-7-3) counterparts from the same outcrop are

215 characterized by higher $\delta^{26}Mg$ values (average of +0.73±0.04‰ for hydrated samples and

216 +0.86±0.17‰ for oxidized samples, 2σ). Silicate mineral separates from veins in the Wadi Fins

217 area are also characterized by $\delta^{26}Mg$ higher than the mantle. Two serpentine veins (OM13-17A

218 WP and OM13-15B) have $\delta^{26}Mg$ values of +0.45‰ and +0.96‰ respectively, and a "waxy vein"

219 (OM15-5-5) with molar Mg/Si of 1, composed of serpentine + stevensite or talc, has a $\delta^{26}Mg$ value

220 of +1.19‰.

221

Figure 3. $\delta^{26}Mg$ (relative to DSM-3) vs. MgO (wt% anhydrous) for harzburgites and dunites.
Black solid line represents the mantle average and dashed black lines encompass the range of
mantle variability (Teng, 2017; Teng et al., 2010).

228 Measured $\delta^{26}Mg$ values in two magnesite listvenites (OM09-11 and OM10-26) are

229 identical and indistinguishable from mantle values (-0.33‰), suggesting nearly isochemical

230 carbonation as inferred from major element ratios by Falk and Kelemen (2015). In contrast, two

231   dolomite listvenites (OM10-14 and OM10-15) are characterized by lower δ^{26}Mg values, -1.46‰

232   and -0.89‰, respectively. Two massive magnesite veins (OM07-39, OM17 Magnesite) record

233   δ^{26}Mg values of -3.14‰ and -3.39‰, or ~3‰ lower than the mantle. Dolomite (OM07-27) and

234   huntite (BA1B 11-2 17-27cm) veins extracted from serpentinized peridotites are also characterized

235   by low δ^{26}Mg values, -1.91‰ and -3.04‰, respectively. Finally, travertines with Mg-rich calcite

236   (OM07-18 and OM07-34A) precipitated from Ca^{2+}-rich hyperalkaline springs (type II waters) are

237   characterized by higher d^{26}Mg than the other carbonates (-1.14‰ and -0.89‰).

238

239   **5. Discussion**

240   *5.1 δ^{26}Mg changes resulting from magnesium mobility*

241

242   The degree of alteration of mantle peridotite can be assessed by looking at deviations from

243   the mantle fractionation produced by melting and melt extraction in a MgO/SiO_2 vs Al_2O_3/SiO_2

244   plot (Figure 4). The mantle fractionation trend is a linear fit to theoretical and observed residues

245   of mantle melting and melt extraction during adiabatic decompression beneath oceanic spreading

246   ridges (Asimow, 1999; Baker and Beckett, 1999; Jagoutz et al., 1979). Based on deviations from

247   the mantle fractionation trend, it is estimated that typical partially serpentinized harzburgites might

248   have lost up to 2 wt% MgO on average (Monnier et al., 2006), though in some cases Si-gain can

249   also lead to decreased MgO/SiO_2 ratios (de Obeso and Kelemen, 2018). Heavily weathered

250   samples within 10 meters of a Cretaceous unconformity in Wadi Fins lost 30% of their initial Mg

251   to the alteration fluid (de Obeso and Kelemen, 2020) and laterites along this unconformity

252   elsewhere in Oman have lost even larger proportions of magnesium (Al-Khirbash, 2016, 2015).

253   Nearly isochemical serpentinization of peridotite (other than H_2O addition) should preserve the

254   MgO/SiO$_2$ ratio of the original protolith, whereas deviations in all of our samples require Mg-loss

255   (Snow and Dick, 1995) and/or Si-addition (de Obeso and Kelemen, 2018). This suggest that open

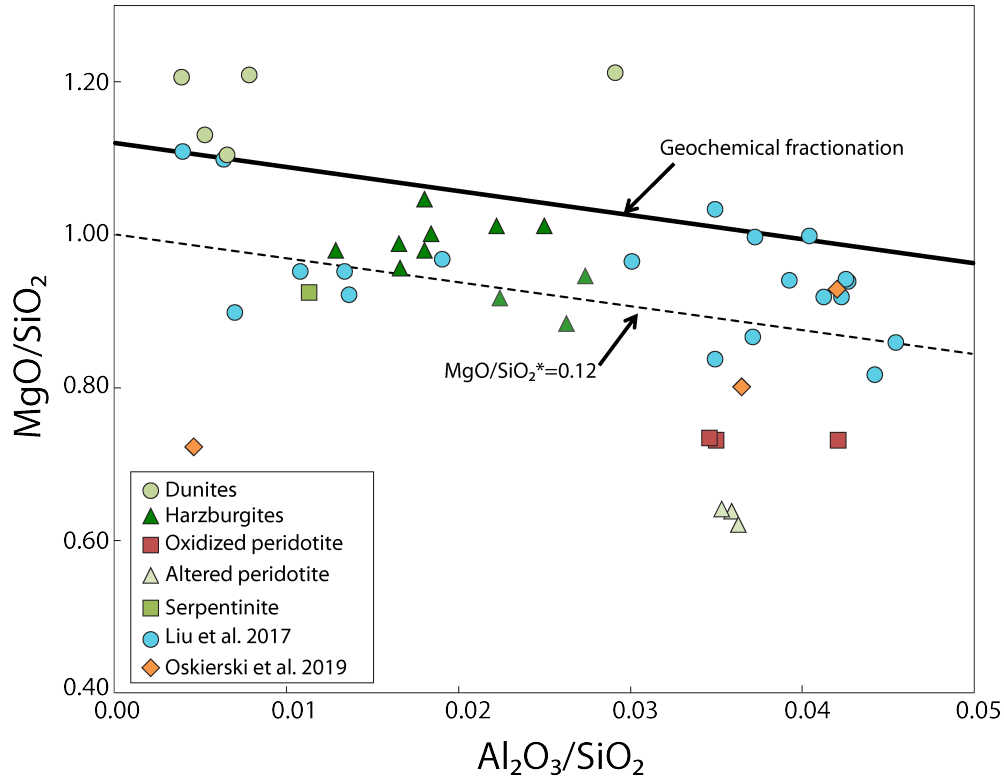256   system mass transfer of major elements has occurred during alteration (Figure 4).

257
258   **Figure 4.** Whole rock MgO/SiO$_2$ vs Al$_2$O$_3$/SiO$_2$ showing sample deviations associated with
259   peridotite alteration from the mantle fractionation trend (bold black line). The mantle
260   fractionation trend is a linear fit to theoretical and observed residues of mantle melting and melt
261   extraction during adiabatic decompression beneath oceanic spreading ridges (Asimow, 1999;
262   Baker and Beckett, 1999). MgO/SiO$_2$*=0.12 shown as dashed black line.
263

264   Furthermore, the presence of meter-wide veins of magnesite in the Samail ophiolite mantle

265   section provides additional evidence of Mg-mobility (Figure 5). However, the veins alone do not

266   indicate if the Mg is derived by minor leaching from a large mass of peridotite, or extensive

267   leaching from a smaller mass. Most analyzed magnesite, dolomite and calcite veins in Samail

268   ophiolite peridotites record measurable ^{14}C, corresponding to ages less than ~ 50ka (Kelemen et

269 al., 2019, 2011; Kelemen and Matter, 2008; Mervine et al., 2014; Streit et al., 2012), suggesting

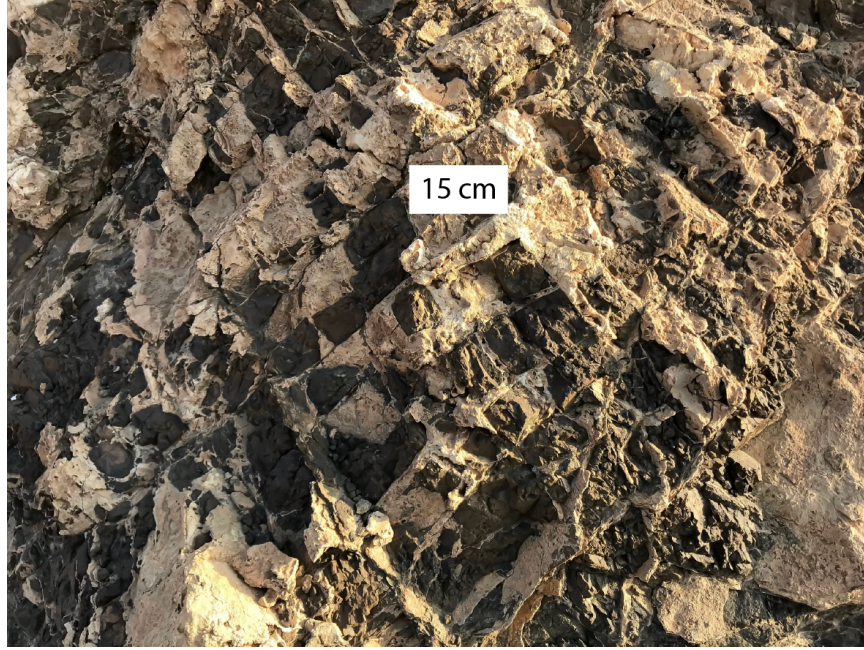270 that some of the alteration associated with Mg mobility is Pleistocene and Holocene.

271

272
273 **Figure 5.** Massive magnesite veins containing angular blocks of serpentinized harzburgite in the
274 Oman ophiolite (UTM 40Q E 671274 N 2536144).
275

276 In order to account for serpentinized harzburgite departures from the geochemical

277 fractionation trend during alteration we use MgO/SiO_2* (Liu et al., 2017; Snow and Dick, 1995)

278 defined as:

279

280
$$\left(\frac{MgO}{SiO_2}\right)^* = \left(-3.15 * \left(\frac{Al_2O_3}{SiO_2}\right)_{sample} + 1.12\right) - \left(\frac{MgO}{SiO_2}\right)_{sample}$$

281

282 All analyzed harzburgites in this study have $\left(\frac{MgO}{SiO_2}\right)^* > 0$ indicative of Mg-loss (Snow and

283 Dick, 1995) and/or Si-addition (de Obeso and Kelemen, 2018) (Figure 5). Samples with $\left(\frac{MgO}{SiO_2}\right)^* <$

284   0.12 are partially serpentinized harzburgites with δ^{26}Mg indistinguishable from the Earth's mantle

285   and BSE (δ^{26}Mg=0.25±0.04‰; Teng, 2017). As $\left(\frac{MgO}{SiO_2}\right)^*$ increases, whole rocks begin to deviate

286   to heavier Mg isotope ratios (Figure 6). Samples with the highest $\left(\frac{MgO}{SiO_2}\right)^*$ in this study are the most

287   enriched in ^{26}Mg and contain Mg-rich clays (de Obeso and Kelemen, 2020). These deviations

288   suggest that 1) variable amounts of Mg have been leached from the peridotites depending on the

289   degree of alteration at different W/R and 2) small Mg depletions are not reflected in δ^{26}Mg of the

290   partially serpentinized harzburgites, which retain mantle-like Mg even at high degrees of
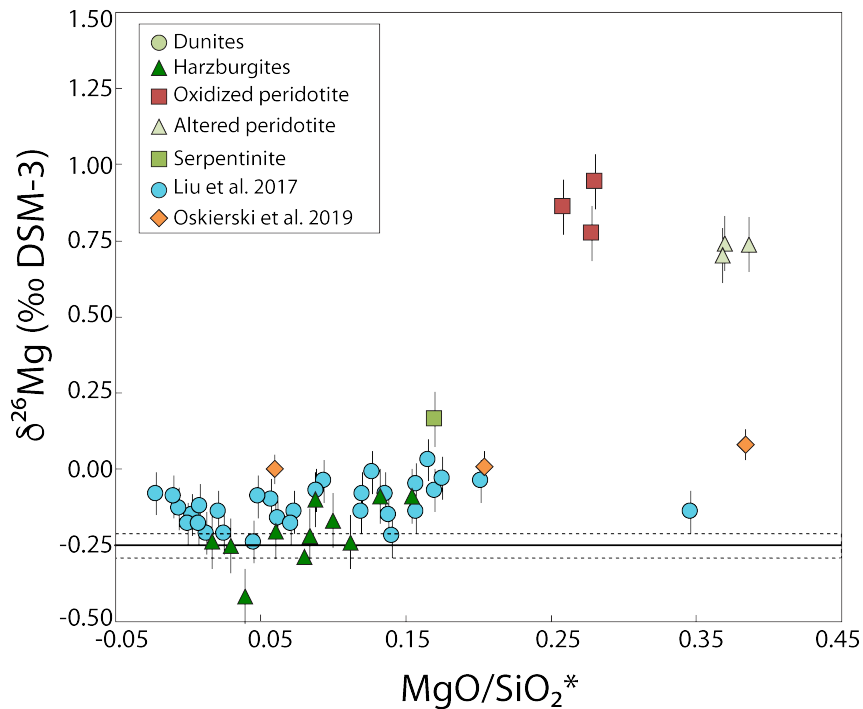
291   serpentinization (e.g. OM13-2 and OM13-19).

292
293
294   **Figure 6.** Bulk rock MgO/SiO$_2$* vs δ^{26}Mg for Oman samples, abyssal peridotites (Liu et al.,
295   2017) and serpentinite (Oskierski et al. 2019). Black solid line is mantle average and dashed
296   black lines delineate the range of variability of mantle compositions (Teng, 2017; Teng et al.,
297   2010).
298

299   We associate the observed Mg mobility with the formation of alteration products in high W/R

300   pathways, including serpentine and carbonates veins with δ^{26}Mg values that depart dramatically

301   from the canonical mantle value. In particular, Mg-carbonates have δ^{26}Mg between -0.64‰ and -

302   3.14‰ lower than unaltered peridotite. Serpentine veins from Wadi Fins are depleted in Fe (Mg#

303   97-98) compared to ambient peridotite (Mg#90), and are interpreted to have formed at high water-

304   to-rock ratios at temperatures between 25-60°C (de Obeso and Kelemen, 2018). Measured δ^{26}Mg

305   values of these serpentine veins are up to 1.2‰ higher than unaltered peridotite. Little or no Mg-

306   isotope fractionation, relative to mantle values, has been found in our whole rock samples of

307   partially serpentinized peridotites, and in previous studies of similar lithologies (Beinlich et al.,

308   2014; Liu et al., 2017). Thus, a different process for the formation of ^{26}Mg-enriched serpentine

309   veins is required. Possibilities include 1) veins were enriched in ^{26}Mg due to isotopic fractionation

310   associated with serpentine precipitation; 2) serpentine precipitated from a fluid enriched in ^{26}Mg

311   due to the removal of ^{24}Mg in other alteration minerals (e.g. carbonates); or 3) some combination

312   of 1) and 2).

313

314   *5.2 Reaction path modeling*

315   *5.2.1   Model setup*

316   To explore the hypothesis that elevated δ^{26}Mg values in serpentine veins are largely the

317   consequence of precipitation from a high δ^{26}Mg fluid, formed by previous fractionation during

318   crystallization of low ^{26}Mg carbonates, we developed a simple reactive transport model that

319   simulates dissolution of primary minerals together with fractional crystallization of serpentine and

320   carbonates based on the reaction path outlined by Barnes and O'Neil (1969) for serpentinization

321   and carbonation systems and modelled by subsequent workers (Bruni et al., 2002; Paukert et al.,

322   2012). We used Paukert et al., (2012) model that reproduces measured aqueous solute

323   concentrations in the peridotite hosted springs via water rock interaction, including co-

324 precipitation of carbonates and serpentine. Most minerals associated with Mg mobility are

325 modelled in the reaction path. This allows us to explore whether the evolution of Mg isotope

326 compositions in alteration minerals during co-precipitation of carbonates and silicates is plausible

327 and consistent with our data.

328

329   This model has three stages. In Stage I, rainwater in equilibrium with the atmosphere

330 infiltrates the peridotite, forming chrysotile, calcite, hydromagnesite and magnetite. The fluid

331 formed in stage I has an Mg^{2+}-HCO_3^- rich composition (Type I). In Stage II, Type I fluid reacts

332 with fresh peridotite isolated from the atmosphere to form magnesium-rich carbonates, chrysotile

333 and brucite, with the fluid evolving to Ca^{2+}-OH^- rich, Mg^{2+}-HCO_3^- poor compositions (Type II)

334 until pH reaches 12 (maximum pH measured in the field). In Stage III (not explicitly modeled by

335 Paukert et al., 2012), Type II fluids emerge on the surface and react with atmospheric CO_2 to form

336 calcite. The model tracks the evolution of $\delta^{26}Mg$ in the resulting fluid and precipitated minerals

337 during each stage. Important model variables and relevant references are given in Table 2. They

338 include initial $\delta^{26}Mg$ fluid compositions, $Mg_{mineral-fluid}$ fractionation factors (α), and the temperature

339 of alteration.

Model parameter	Value	Reference
Temperature	30°C	Weyhenmeyer et al., 2002
Magnesite $\alpha_{mgs-fluid}$	0.9972	Wang et al 2019
	0.9954	Schauble et al. 2011
	0.9979	Schott et al. 2016^
Dolomite $\alpha_{dol-fluid}$	0.9972	Wang et al. 2019
	0.9954	Schauble et al. 2011
	0.9979	Li et al. 2015
Hydromagnesite $\alpha_{hmgs-fluid}$	0.9990	Shirokova et al. 2013
Initial $\delta^{26}Mg$ fluid	-2.0‰	Teng, 2017
$[Mg]_0$ fluid	7.7×10^{-5} molal	Paukert et al. 2012
Peridotite $\delta^{26}Mg$	-0.25‰	Teng, 2017
[Mg] peridotite	28.4 wt%	Paukert et al. 2012

^ Schott is extrapolated from batch reaction data

340   **Table 2.** Model parameters

341   Equilibrium isotope fractionation of Mg isotopes is temperature dependent (Li et al., 2015;

342   Pinilla et al., 2015; Ryu et al., 2016; Schott et al., 2016; Wang et al., 2019), rendering temperature

343   estimates important for understanding alteration. For calculations in this paper, we used 30°C,

344   approximately the current annual average temperature in the northern Oman mountains

345   (Weyhenmeyer et al., 2002). This temperature is consistent with other constraints established in

346   studies of most of the samples analyzed in this study. de Obeso and Kelemen (2018) estimated that

347   alteration in Wadi Fins occurred between 25-60°C based on clumped isotope thermometry of

348   carbonate veins in peridotite. Carbonate veins in typical, partially serpentinized mantle peridotites

349   in the Samail ophiolite also yield crystallization temperatures between 25-50°C, calculated using

350   both $\delta^{18}O$ exchange and clumped isotope thermometry (Kelemen et al., 2011; Streit et al., 2012).

351

352   Our model assumes that products of nearly isochemical, olivine serpentinization do not

353   fractionate Mg isotopes from the fluid (α=1.0000 for serpentine and brucite) as concluded in

354   previous studies of natural samples (Beinlich et al., 2014; Liu et al., 2017). The preferential

355   incorporation of ^{24}Mg in carbonates, reported both in experimental and field observations (Higgins

356   and Schrag, 2010; Li et al., 2015; Mavromatis et al., 2013; Pearce et al., 2012; Shirokova et al.,

357   2013; Tipper et al., 2006), is a critical factor in our model. This isotopic fractionation is largely

358   responsible for producing the fluid with high $\delta^{26}Mg$, that then produces serpentine veins with

359   heavy Mg. We used carbonate-fluid fractionation factors (α) from empirical and experimental

360   studies. For hydromagnesite, we used a fractionation factor of α=0.9990, derived from low

361   temperature precipitation experiments on alkaline natural water of Salda Lake, Turkey (Shirokova

362   et al., 2013). We prefer this value to the only other published value for hydromagnesite (Oelkers

363   et al., 2018), because the latter group attributed their results to disequilibrium processes. For

364   magnesite and dolomite we used a range of fractionation factors reported in the literature, as listed

365   in Table 2. Precipitation kinetics of magnesite and dolomite at low temperatures are poorly

366   understood (Arvidson and Mackenzie, 1999; Saldi et al., 2012). Dolomite crystallization has not

367   been achieved in laboratory conditions, even after a three decade long experiment (Land, 1998),

368   and until 2017 magnesite had not been experimentally crystallized at temperatures below 60°C

369   (e.g., Hänchen et al., 2008; Johnson et al., 2014), though more recent work produced magnesite at

370   room temperature from fluids enriched in organic ligands (Power et al., 2017). In our models,

371   magnesite-water fractionation factors at 30°C were extrapolated from higher temperature

372   experiments (Li et al., 2015; Schott et al., 2016) or derived from first principles estimates and

373   molecular dynamics (Schauble, 2011; Wang et al., 2019). Mg fractionation between calcite and

374   fluid depends on multiple factors in addition to temperature (Li et al., 2012), including Mg content

375   (Wang et al., 2019) and precipitation rate (Mavromatis et al., 2013). Fractionation factors for

376   calcite are not directly used in the model.

377

378   The first two stages of the reaction path model yield calculated Mg isotope compositions

379   of the fluid and precipitated minerals as a function of reaction progress, quantified using the

380   water/rock ratio (W/R). We used the fractionation factors described above, and a model of

381   assimilation and fractional crystallization (AFC) (DePaolo, 1981). The primary minerals (olivine,

382   orthopyroxene and clinopyroxene) in the model have δ^{26}Mg of -0.25‰. At each step of the model,

383   primary minerals are dissolved and secondary minerals (chrysotile + hydromagnesite in Stage I,

384   chrysotile + brucite + dolomite and magnesite in Stage II) are allowed to precipitate. We assume

385   that the starting Mg isotope composition in the fluid for the first stage is in equilibrium with the

386   late Cretaceous to Eocene limestones that locally overlie the ophiolite, with initial δ^{26}Mg$_{fluid}$ of -

387   2.0‰. Values for $\delta^{26}Mg_{fluid}$ at each model step are calculated using the AFC equation for stable

388   isotopes:

389

390    $$\delta_f - \delta_f^0 = \left(\frac{r}{r-1}\right)\frac{C_a}{zC_f}\left[\delta_a - \delta_f^0 - \frac{D\Delta}{z(r-1)}\right]X(1-F^{-z}) - \frac{D\Delta}{(r-1)}lnF\left[1-\left(\frac{r}{r-1}\right)\frac{C_a}{zC_f}\right]$$

391

392   where δ_f and δ_a are the $\delta^{26}Mg$ of the fluid and the primary minerals respectively, Δ =1000 $ln\alpha_{mineral-}$

393    $_{fluid}$, r is the ratio of mass assimilated over mass precipitated, D is the bulk partition coefficient

394   between secondary minerals and fluid, C_f is the Mg concentration in the fluid, C_a is the Mg

395   concentration in the primary minerals, z=(r+D-1)/(r-1) and F is the ratio of fluid mass to initial

396   fluid mass. $\Delta^{26}Mg$ of secondary minerals is calculated in each step using the fluid Mg isotope

397   compositions and precipitated minerals fractionation factors ($\alpha_{mineral-fluid}$).

398

399   *5.2.2   Model results*

400   In Stage I, small extents of water-rock interaction (high W/R) cause fluid evolution from

401   the initial $\delta^{26}Mg$ of -2‰ to a value of -0.25‰ (Figure 7). During precipitation of hydromagnesite,

402   the fluid becomes slightly enriched in heavy isotopes before reaching a steady state at $\delta^{26}Mg$=-

403   0.15‰ with W/R less than 100. The evolved fluid is Mg-HCO$_3$ rich.

404

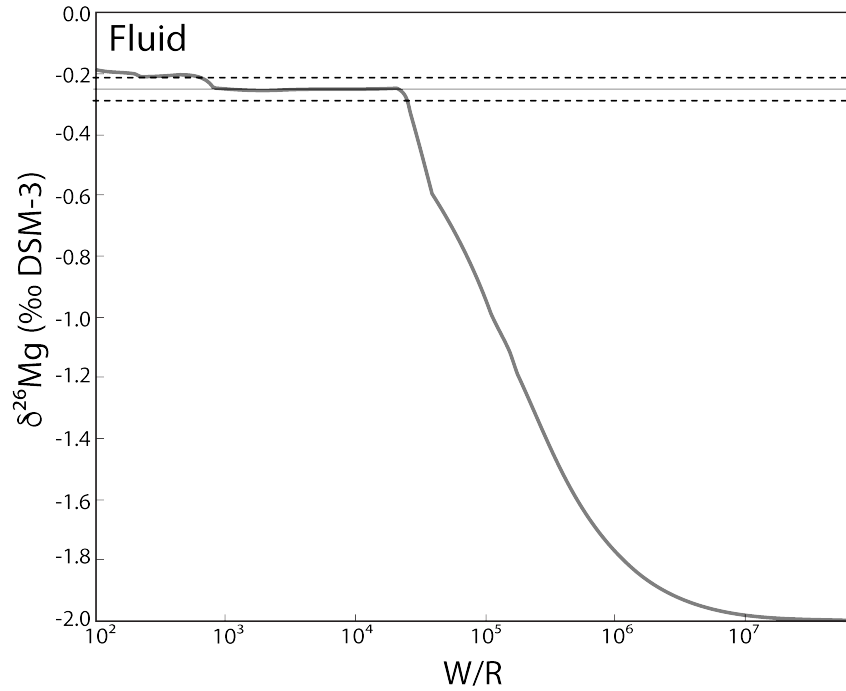**Figure 7.** δ^{26}Mg evolution of the fluid in the first stage of reaction, open to gas exchange with the atmosphere. Black solid line is mantle average and dashed black lines delineate the range of variability of mantle compositions (Teng, 2017; Teng et al., 2010).

In Stage II, the Mg-HCO$_3$ rich fluid evolves to Mg- and C-depleted waters with high Ca^{2+} and pH as well as extremely low fO$_2$. Mineral precipitation is dominated by formation of magnesite and chrysotile with minor dolomite, at W/R between 2000-100,000 (Figure 8). Mg-rich carbonates begin to precipitate with their lightest δ^{26}Mg values, and evolve to heavier compositions as W/R decreases (Figure 8c and 8d). The precipitation of Mg-rich carbonates drives fluid and serpentine to heavier δ^{26}Mg (Figure 8b). Once the system becomes carbon-depleted, and magnesite disappears from the crystallizing mineral assemblage at W/R~1800, the fluid/serpentine system rapidly evolves to mantle-like isotope ratios (Figure 8b) while dolomite also disappears from the system (Figure 8d).
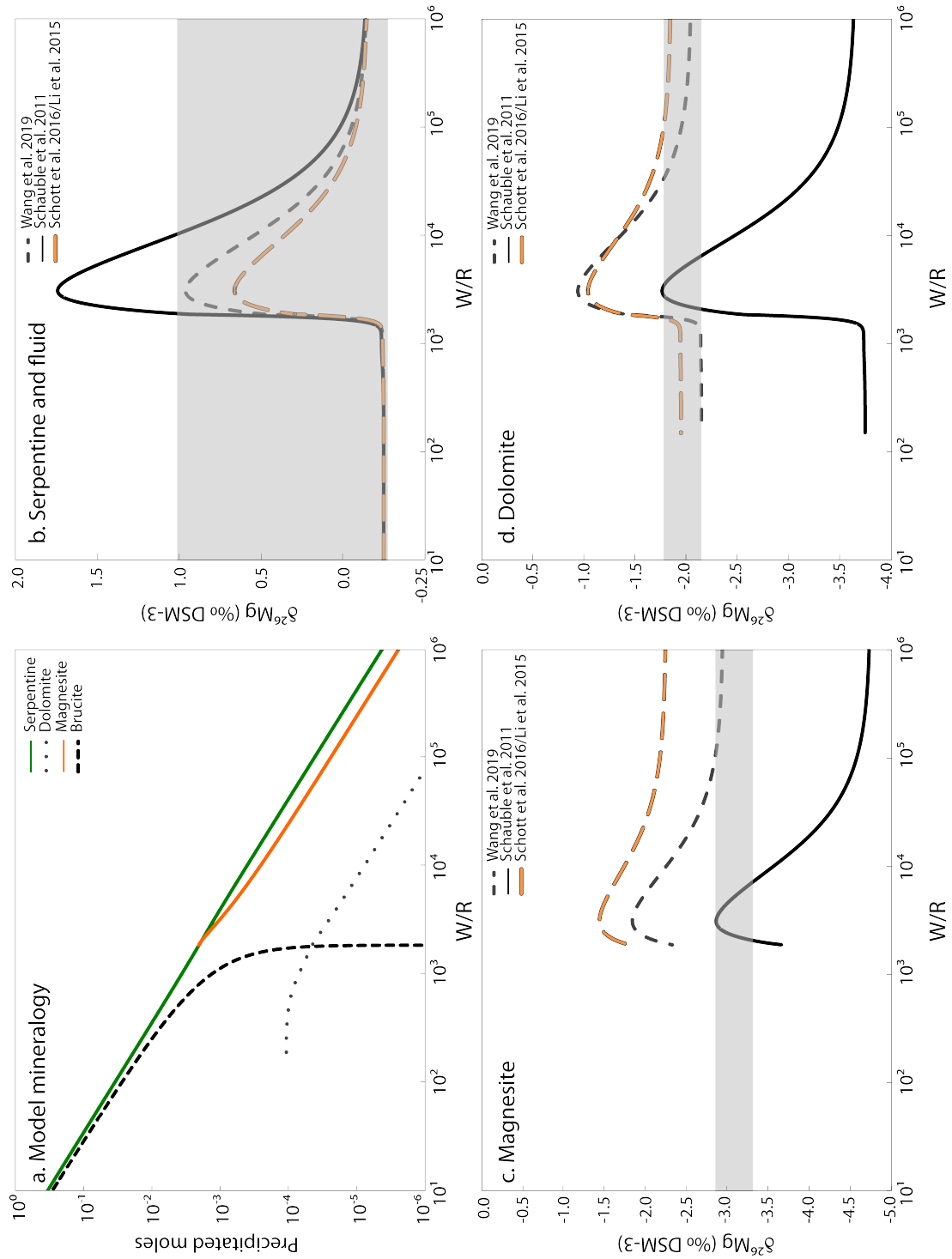
Figure 8. Results from the second stage of the reaction path model, closed to exchange with the atmosphere, illustrating mineral products (a), $\delta^{26}Mg$ of fluid and serpentine (b), magnesite (c), and dolomite (d). Grey squares illustrate the observed range of sample values for each mineral.

427   Given the range of model variables listed in Table 2, this model is able to explain three

428   aspects of our Mg isotope data – 1) low δ^{26}Mg in massive carbonate veins, 2) high δ^{26}Mg in

429   serpentine veins and some heavily weathered bulk rock samples, and 3) δ^{26}Mg of partially altered

430   serpentinites that are indistinguishable from mantle values. The light values reflect co-precipitation

431   of serpentine and carbonate at high W/R ratios. As W/R decreases, carbonates disappear from the

432   crystallizing assemblage, the fluid evolves to δ^{26}Mg=-0.25‰, and precipitated serpentine also has

433   mantle-like Mg isotope ratios, consistent with observed values in this and other studies (Beinlich

434   et al., 2014; Liu et al., 2017). While the carbonate and serpentine samples in this study come from

435   a broad region, and are not specifically co-genetic, our measurements show how serpentine veins

436   can have magnesium isotopic ratios different from those of the protolith, even when serpentine-

437   water exchange itself does not fractionate Mg-isotopes.

438

439   In the natural system, the Type II hyper-alkaline Ca-rich fluid comes in contact with the

440   atmosphere in springs, where it combines with CO_2 from air to form extensive travertine deposits

441   (Chavagnac et al., 2013a; Clark and Fontes, 1990; Kelemen et al., 2011; Kelemen and Matter,

442   2008; Mervine et al., 2014; Neal and Stanger, 1985). Travertines analyzed in this study have δ^{26}Mg

443   of -1.14‰ and -0.89‰. In our modeling, at pH 12 the fluid has an isotope ratio identical to mantle

444   values, δ^{26}Mg=-0.25‰. If calcite in travertines precipitated from this fluid, then the inferred

445   Δ^{26}Mg$_{cal-fl}$ of the travertine must have been lower than the value of ~3‰ expected for equilibrium

446   fractionation with such a fluid (Li et al., 2012; Mavromatis et al., 2017; Wang et al., 2019). Indeed,

447   Mavromatis et al. (2013) showed that Δ^{26}Mg$_{cal-fl}$ is dependent on the growth rate of calcite, with

448   Δ^{26}Mg$_{cal-fl}$ (δ^{26}Mg$_{cal}$ − δ^{26}Mg$_{fl}$) decreasing with increasing growth rate. (This type of growth rate

449   dependence has not been reported for magnesite or dolomite). The inferred Δ^{26}Mg$_{cal-fl}$ for calcite

450   in Oman travertines suggests calcite growth rates of $\sim 10^{-5}$ mol/(m²s). Such rapid growth is

451   consistent with the non-equilibrium, high Mg contents in peridotite-hosted travertines in the

452   Samail ophiolite and other massifs (e.g. Barnes and O'Neil, 1971, 1969; Chavagnac et al., 2013;

453   Kelemen et al., 2011; Kelemen and Matter, 2008; Streit et al., 2012). Assuming that 1 to 10% of

454   the total estimated travertine area in the Samail ophiolite ($\sim 10^7$ m² (Kelemen and Matter, 2008))

455   is actively precipitating, this rate yields a total uptake of 10^3-10^4 tons atmospheric CO_2/yr, similar

456   to previous estimates of carbon uptake to form travertine in the ophiolite (Kelemen et al., 2011;

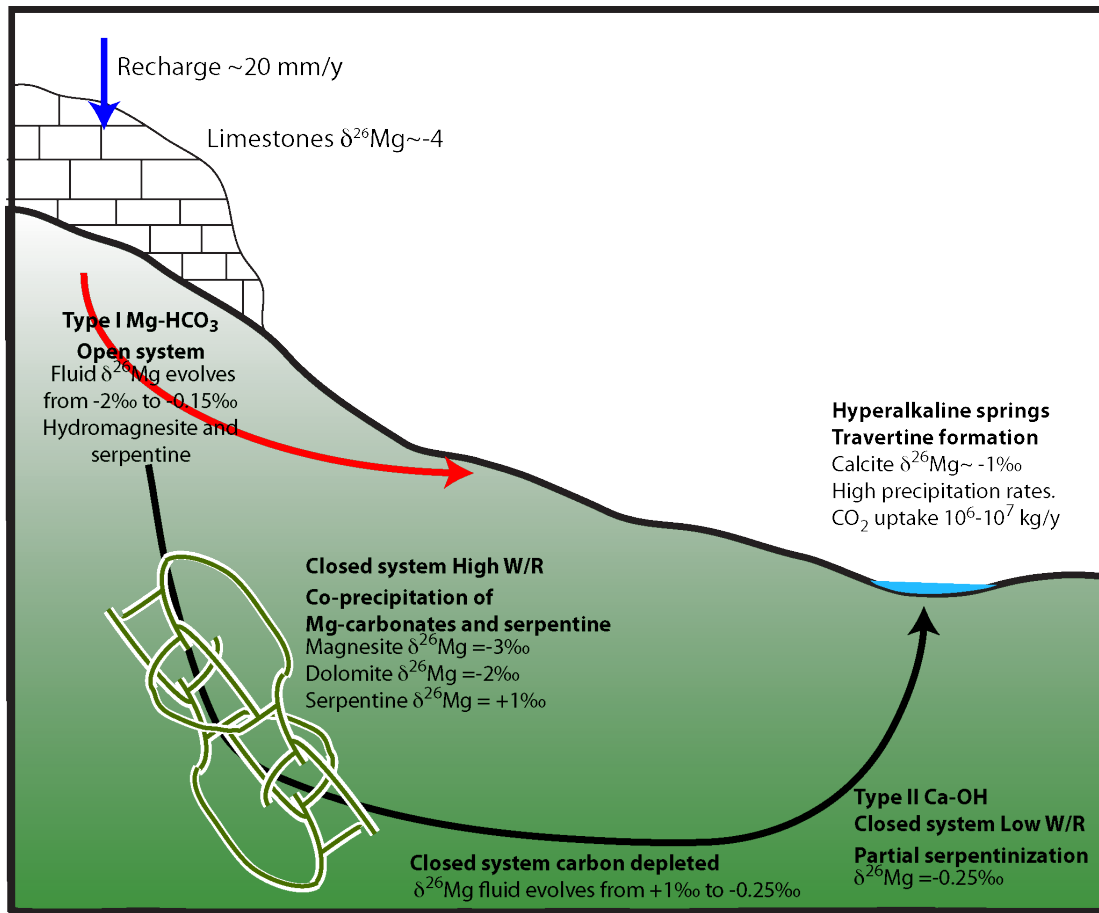457   Kelemen and Matter, 2008; Mervine et al., 2014), as shown schematically in figure 9.

Figure 9. Conceptual model of Mg isotope systematics in the modern alteration system in Oman (after Dewandel et al., 2005; Neal and Stanger, 1985).

464   **6. Conclusions**

465   Most partially serpentinized dunites and harzburgites in the mantle section of the Samail

466   ophiolite have δ^{26}Mg indistinguishable from average mantle values. Serpentinization at low W/R

467   does not fractionate Mg isotopes. However, deviations from mantle δ^{26}Mg are observed in rocks

468   which have undergone extensive Mg leaching at higher W/R. Heavily altered peridotites recording

469   up to 30% Mg loss, and containing Mg-clay minerals, have the heaviest δ^{26}Mg ever reported for

470   ultramafic rocks. We model a mechanism in which Mg-rich carbonates precipitate at high W/R,

471   preferentially incorporating ^{24}Mg and producing ^{26}Mg-rich fluids that then precipitate serpentine

472   veins with heavy Mg. When carbonates disappear from the crystallizing assemblage at lower W/R,

473   serpentine evolves to mantle-like δ^{26}Mg. The modelled δ^{26}Mg for serpentine formed along with

474   carbonates is similar to observed δ^{26}Mg in serpentine vein samples. The fact that most peridotite-

475   hosted carbonate veins have finite ^{14}C ages, along with our modelling results, is consistent with

476   other observations indicating that serpentinization and carbonation are ongoing in Oman. The

477   proposed mechanism can be further explored using co-genetic carbonate-serpentine veins from the

478   newly drilled cores from the Oman Drilling Project. δ^{26}Mg in calcite forming travertine deposits

479   at peridotite-hosted alkaline springs is heavier than expected from equilibrium fractionation

480   between calcite and fluid with mantle-like Mg isotope ratios, suggesting rapid, disequilibrium

481   crystallization. We infer calcite growth rates of 10^{-5} mol/m^{2}s, corresponding to uptake of

482   atmospheric CO_2 at a rate of 10^6-10^7 kg CO_2/yr to form travertine in Oman.

486 Foundation – Deep Carbon Observatory (Grant 2014-3-01, Kelemen PI), the U.S.-National

487 Science Foundation (NSF-EAR-1516300, Kelemen lead PI). All geochemical data for this work

488 will be uploaded to PetDB (http://www.earthchem.org/petdb) and is included with the manuscript

489 for the review process.

490

491

References

493 Al-Khirbash, S., 2016. Geology, mineralogy, and geochemistry of low grade Ni-lateritic soil
494   (Oman Mountains, Oman). Chemie der Erde - Geochemistry.
495   https://doi.org/10.1016/j.chemer.2016.08.002

496 Al-Khirbash, S., 2015. Genesis and mineralogical classification of Ni-laterites, Oman Mountains.
497   Ore Geol. Rev. 65, 199–212. https://doi.org/10.1016/j.oregeorev.2014.09.022

498 Arvidson, R.S., Mackenzie, F.T., 1999. The dolomite problem; control of precipitation kinetics
499   by temperature and saturation state. Am. J. Sci. 299, 257–288.
500   https://doi.org/10.2475/ajs.299.4.257

501 Asimow, P.D., 1999. A model that reconciles major- and trace-element data from abyssal
502   peridotites. Earth Planet. Sci. Lett. 169, 303–319. https://doi.org/10.1016/S0012-
503   821X(99)00084-9

504 Auclair, M., Gauthier, M., Trottier, J., Jebrak, M., Chartrand, F., 1993. Mineralogy,
505   geochemistry, and paragenesis of the Eastern Metals serpentinite-associated Ni-Cu-Zn
506   deposit, Quebec Appalachians. Econ. Geol. 88, 123–138.
507   https://doi.org/10.2113/gsecongeo.88.1.123

508 Baker, M.B., Beckett, J.R., 1999. The origin of abyssal peridotites: a reinterpretation of
509   constraints based on primary bulk compositions. Earth Planet. Sci. Lett. 171, 49–61.
510   https://doi.org/https://doi.org/10.1016/S0012-821X(99)00130-2

511 Barnes, I., LaMarche, V.C., Himmelberg, G., 1967. Geochemical Evidence of Present-Day
512   Serpentinization. Science (80-.). 156, 830–832.
513   https://doi.org/10.1126/science.156.3776.830

514 Barnes, I., O'Neil, J.R., 1971. Calcium-magnesium carbonate solid solutions from Holocene
515   conglomerate cements and travertines in the Coast Range of California. Geochim.
516   Cosmochim. Acta 35, 699–718. https://doi.org/10.1016/0016-7037(71)90068-8

517 Barnes, I., O'Neil, J.R., 1969. The Relationship between Fluids in Some Fresh Alpine-Type
518   Ultramafics and Possible Modern Serpentinization, Western United States. Geol. Soc. Am.
519   Bull. 80, 1947. https://doi.org/10.1130/0016-7606(1969)80[1947:TRBFIS]2.0.CO;2

520 Barnes, I., O'Neil, J.R., Trescases, J.., 1978. Present day serpentinization in New Caledonia,
521   Oman and Yugoslavia. Geochim. Cosmochim. Acta 42, 144–145.

522 https://doi.org/10.1016/0016-7037(78)90225-9

523 Beinlich, A., Austrheim, H., Mavromatis, V., Grguric, B., Putnis, C. V., Putnis, A., 2018.
524   Peridotite weathering is the missing ingredient of Earth's continental crust composition.
525   Nat. Commun. 9. https://doi.org/10.1038/s41467-018-03039-9

526 Beinlich, A., Mavromatis, V., Austrheim, H., Oelkers, E.H., 2014. Inter-mineral Mg isotope
527   fractionation during hydrothermal ultramafic rock alteration – Implications for the global
528   Mg-cycle. Earth Planet. Sci. Lett. 392, 166–176. https://doi.org/10.1016/j.epsl.2014.02.028

529 Boudier, F., Coleman, R.G., 1981. Cross section through the peridotite in the Samail ophiolite,
530   southeastern Oman Mountains. J. Geophys. Res. Solid Earth 86, 2573–2592.
531   https://doi.org/10.1029/JB086iB04p02573

532 Braun, M.G., 2004. Petrologic and Microstructural Constraints on Focused Melt Transport in
533   Dunites and Rheology of the Shallow Mantle. WHOI/MIT.

534 Braun, M.G., Kelemen, P.B., 2002. Dunite distribution in the Oman Ophiolite: Implications for
535   melt flux through porous dunite conduits. Geochemistry, Geophys. Geosystems 3, 1–21.
536   https://doi.org/10.1029/2001GC000289

537 Bruni, J., Canepa, M., Chiodini, G., Cioni, R., Cipolli, F., Longinelli, A., Marini, L., Ottonello,
538   G., Vetuschi Zuccolini, M., 2002. Irreversible water–rock mass transfer accompanying the
539   generation of the neutral, Mg–HCO3 and high-pH, Ca–OH spring waters of the Genova
540   province, Italy. Appl. Geochemistry 17, 455–474. https://doi.org/10.1016/S0883-
541   2927(01)00113-5

542 Chavagnac, V., Ceuleneer, G., Monnin, C., Lansac, B., Hoareau, G., Boulart, C., 2013a.
543   Mineralogical assemblages forming at hyperalkaline warm springs hosted on ultramafic
544   rocks: A case study of Oman and Ligurian ophiolites. Geochemistry, Geophys. Geosystems
545   14, 2474–2495. https://doi.org/10.1002/ggge.20146

546 Chavagnac, V., Monnin, C., Ceuleneer, G., Boulart, C., Hoareau, G., 2013b. Characterization of
547   hyperalkaline fluids produced by low-temperature serpentinization of mantle peridotites in
548   the Oman and Ligurian ophiolites. Geochemistry, Geophys. Geosystems 14, 2496–2522.
549   https://doi.org/10.1002/ggge.20147

550 Clark, I.D., Fontes, J.-C., 1990. Paleoclimatic reconstruction in northern Oman based on
551   carbonates from hyperalkaline groundwaters. Quat. Res. 33, 320–336.
552   https://doi.org/10.1016/0033-5894(90)90059-T

553 Coleman, R.G., Keith, T.E., 1971. A Chemical Study of Serpentinization — Burro Moutain,
554   California. J. Petrol. 12, 311–328.

555 Collier, M.L., 2012. Spatial-Statistical Properties of Geochemical Variability as Constraints on
556   Magma Transport and Evolution Processes at Ocean Ridges. Columbia University.

557 de Obeso, J.C., Kelemen, P.B., 2020. Major element mobility during serpentinization, oxidation
558   and weathering of mantle peridotite at low temperatures. Philos. Trans. A. Math. Phys. Eng.
559   Sci. 378, 20180433. https://doi.org/10.1098/rsta.2018.0433

560 de Obeso, J.C., Kelemen, P.B., 2018. Fluid rock interactions on residual mantle peridotites
561   overlain by shallow oceanic limestones: Insights from Wadi Fins, Sultanate of Oman.
562   Chem. Geol. https://doi.org/10.1016/J.CHEMGEO.2018.09.022

563 DePaolo, D.J., 1981. Trace element and isotopic effects of combined wallrock assimilation and
564   fractional crystallization. Earth Planet. Sci. Lett. 53, 189–202. https://doi.org/10.1016/0012-
565   821X(81)90153-9

566 Esteban Guzman, J., Cuevas Urionabarrenechea, J., Tubía Martínez, J., Velasco Roldán, F.,
567   Vegas Tubia, N., 2011. Características petrográficas y mineralógicas de birbiritas derivadas
568   de las peridotitas de Ronda (Cordilleras Béticas). Geogaceta 39–42.

569 Falk, E.S., Kelemen, P.B., 2015. Geochemistry and petrology of listvenite in the Samail
570   ophiolite, Sultanate of Oman: Complete carbonation of peridotite during ophiolite
571   emplacement. Geochim. Cosmochim. Acta 160, 70–90.
572   https://doi.org/10.1016/j.gca.2015.03.014

573 Frost, R.B., 1985. On the stability of sulfides, oxides, and native metals in serpentinite. J. Petrol.
574   26, 31–63. https://doi.org/10.1093/petrology/26.1.31

575 Galy, A., Belshaw, N.S., Halicz, L., O'Nions, R.K., 2001. High-precision measurement of
576   magnesium isotopes by multiple-collector inductively coupled plasma mass spectrometry.
577   Int. J. Mass Spectrom. 208, 89–98. https://doi.org/10.1016/S1387-3806(01)00380-3

578 Galy, A., Yoffe, O., Janney, P.E., Williams, R.W., Cloquet, C., Alard, O., Halicz, L., Wadhwa,
579   M., Hutcheon, I.D., Ramon, E., Carignan, J., 2003. Magnesium isotope heterogeneity of the
580   isotopic standard SRM980 and new reference materials for magnesium-isotope-ratio
581   measurements. J. Anal. At. Spectrom. 18, 1352–1356. https://doi.org/10.1039/B309273A

582 Gao, C., Cao, X., Liu, Q., Yang, Y., Zhang, S., He, Y., Tang, M., Liu, Y., 2018. Theoretical
583   calculation of equilibrium Mg isotope fractionations between minerals and aqueous
584   solutions. Chem. Geol. 488, 62–75. https://doi.org/10.1016/J.CHEMGEO.2018.04.005

585 Godard, M., Jousselin, D., Bodinier, J.-L., 2000. Relationships between geochemistry and
586   structure beneath a palaeo-spreading centre: a study of the mantle section in the Oman
587   ophiolite. Earth Planet. Sci. Lett. 180, 133–148. https://doi.org/10.1016/S0012-
588   821X(00)00149-7

589 Gregory, R.T., Taylor, H.P., 1981. An Oxygen Isotope Profile in a Section of Cretaceous
590   Oceanic Crust, Samail Ophiolite, Oman: Evidence for δ18O Buffering of the Oceans
591   Circulation at Mid-Ocean Ridges. J. Geophys. Res. 86, 2737–2755.

592 Hänchen, M., Prigiobbe, V., Baciocchi, R., Mazzotti, M., 2008. Precipitation in the Mg-
593   carbonate system—effects of temperature and CO2 pressure. Chem. Eng. Sci. 63, 1012–
594   1028. https://doi.org/10.1016/J.CES.2007.09.052

595 Hanghøj, K., Kelemen, P.B., Hassler, D., Godard, M., 2010. Composition and Genesis of
596   Depleted Mantle Peridotites from the Wadi Tayin Massif, Oman Ophiolite; Major and
597   Trace Element Geochemistry, and Os Isotope and PGE Systematics. J. Petrol. 51, 201–227.
598   https://doi.org/10.1093/petrology/egp077

599 Higgins, J.A., Schrag, D.P., 2010. Constraining magnesium cycling in marine sediments using
600   magnesium isotopes. Geochim. Cosmochim. Acta 74, 5039–5053.
601   https://doi.org/10.1016/j.gca.2010.05.019

602 Hotz, P.E., 1964. Nickeliferous laterites in southwestern Oregon and northwestern California.
603   Econ. Geol. 59, 355–396. https://doi.org/10.2113/gsecongeo.59.3.355

604 Husson, J.M., Higgins, J.A., Maloof, A.C., Schoene, B., 2015. Ca and Mg isotope constraints on
605   the origin of Earth's deepest δ13C excursion. Geochim. Cosmochim. Acta 160, 243–266.
606   https://doi.org/10.1016/j.gca.2015.03.012

607 Jagoutz, E., Palme, H., Baddenhausen, H., Blum, K., Cendales, M., Dreibus, G., Spettel, B.,
608   Lorenz, V., Wanke, H., 1979. The abundances of major, minor and trace elements in the
609   earth's mantle as derived from primitive ultramafic nodules, in: Proceedings of the Lunar
610   and Planetary Science Conference 10. pp. 2031–2050.

611 Johnson, N.C., Thomas, B., Maher, K., Rosenbauer, R.J., Bird, D., Brown, G.E., 2014. Olivine
612   dissolution and carbonation under conditions relevant for in situ carbon storage. Chem.
613   Geol. 373, 93–105. https://doi.org/10.1016/J.CHEMGEO.2014.02.026

614 Kelemen, P.B., de Obeso, J.C., Manning, C., Godard, M., Bach, W., Cai, Y., Choe, S., Coggon,
615   J., Ellison, E., Eslami, A., Evans, K., Harris, M., Kahl, W.-A., Matter, J., Michibayashi, K.,
616   Okazaki, K., Pezard, P., Teagle, D., Templeton, A., OmanDP Science Team, Team, O.S.,
617   2019. Peridotite alteration in OmanDP cores, in: Geophysical Research Abstracts. pp.
618   EGU2019-17259.

619 Kelemen, P.B., Matter, J.M., 2008. In situ carbonation of peridotite for CO2 storage. Proc. Natl.
620   Acad. Sci. 105, 17295–17300. https://doi.org/10.1073/pnas.0805794105

621 Kelemen, P.B., Matter, J.M., Streit, E.E., Rudge, J.F., Curry, W.B., Blusztajn, J., 2011. Rates and
622   Mechanisms of Mineral Carbonation in Peridotite: Natural Processes and Recipes for
623   Enhanced, in situ CO 2 Capture and Storage. Annu. Rev. Earth Planet. Sci. 39, 545–576.
624   https://doi.org/10.1146/annurev-earth-092010-152509

625 Kelemen, P.B., Matter, J.M., Teagle, D.A.H., Coggon, J.A. (Eds.), 2020. Proceedings of the
626   Oman Drilling Project, Proceedings of the International Ocean Discovery Program.
627   International Ocean Discovery Program. https://doi.org/10.14379/OmanDP.proc.2020

628 Land, L., 1998. Failure to Precipitate Dolomite at 25° C from Dilute Solution Despite 1000-Fold
629   Oversaturation after 32 Years. Aquat. Geochemistry 361–368.

630 Li, W., Beard, B.L., Li, C., Xu, H., Johnson, C.M., 2015. Experimental calibration of Mg isotope
631   fractionation between dolomite and aqueous solution and its geological implications.
632   Geochim. Cosmochim. Acta 157, 164–181.

633 Li, W., Chakraborty, S., Beard, B.L., Romanek, C.S., Johnson, C.M., 2012. Magnesium isotope
634   fractionation during precipitation of inorganic calcite under laboratory conditions. Earth
635   Planet. Sci. Lett. 333–334, 304–316. https://doi.org/10.1016/J.EPSL.2012.04.010

636 Liu, P.-P., Teng, F.-Z., Dick, H.J.B., Zhou, M.-F., Chung, S.-L., 2017. Magnesium isotopic
637   composition of the oceanic mantle and oceanic Mg cycling. Geochim. Cosmochim. Acta
638   206, 151–165. https://doi.org/10.1016/j.gca.2017.02.016

639 Lorand, J.P., 1988. Fe   Ni   Cu sulfides in tectonite peridotites from the Maqsad district, Sumail
640   ophiolite, southern Oman: Implications for the origin of the sulfide component in the
641   oceanic upper mantle. Tectonophysics 151, 57–73. https://doi.org/10.1016/0040-
642   1951(88)90240-5

643 Malvoisin, B., 2015. Mass transfer in the oceanic lithosphere: Serpentinization is not
644   isochemical. Earth Planet. Sci. Lett. 430, 75–85. https://doi.org/10.1016/j.epsl.2015.07.043

Mavromatis, V., Gautier, Q., Bosc, O., Schott, J., 2013. Kinetics of Mg partition and Mg stable isotope fractionation during its incorporation in calcite. Geochim. Cosmochim. Acta 114, 188–203. https://doi.org/10.1016/J.GCA.2013.03.024

Mavromatis, V., Purgstaller, B., Dietzel, M., Buhl, D., Immenhauser, A., Schott, J., 2017. Impact of amorphous precursor phases on magnesium isotope signatures of Mg-calcite. Earth Planet. Sci. Lett. 464, 227–236. https://doi.org/10.1016/J.EPSL.2017.01.031

Mervine, E.M., Humphris, S.E., Sims, K.W.W., Kelemen, P.B., Jenkins, W.J., 2014. Carbonation rates of peridotite in the Samail Ophiolite, Sultanate of Oman, constrained through 14C dating and stable isotopes. Geochim. Cosmochim. Acta 126, 371–397. https://doi.org/10.1016/j.gca.2013.11.007

Monnier, C., Girardeau, J., Le Mée, L., Polvé, M., 2006. Along-ridge petrological segmentation of the mantle in the Oman ophiolite. Geochemistry, Geophys. Geosystems 7, n/a-n/a. https://doi.org/10.1029/2006GC001320

Monnin, C., Chavagnac, V., Ceuleneer, G., Boulart, C., Hoareau, G., 2011. Characterization of hyperalkaline fluids produced by serpentinization of mantle peridotites in Oman and in Liguria (Northern Italy). Mineral. Mag 75, 1490.

Moody, J.B., 1976. Serpentinization: a review. Lithos 9, 125–138. https://doi.org/10.1016/0024-4937(76)90030-X

Nasir, S., Al Sayigh, A.R., Al Harthy, A., Al-Khirbash, S., Al-Jaaidi, O., Musllam, A., Al-Mishwat, A., Al-Bu'saidi, S., 2007. Mineralogical and geochemical characterization of listwaenite from the Semail Ophiolite, Oman. Chemie der Erde - Geochemistry 67, 213–228. https://doi.org/10.1016/j.chemer.2005.01.003

Neal, C., Stanger, G., 1985. Past and present serpentinization of ultramafic rocks: An example from the Semail ophiolite nappe of northern Oman, in: Drewer, J. (Ed.), The Chemistry of Weathering. D. Reidel Publishing Company, Dordrecht, Holland, pp. 249–275.

Neal, C., Stanger, G., 1983. Hydrogen generation from mantle source rocks in Oman. Earth Planet. Sci. Lett. 66, 315–320. https://doi.org/10.1016/0012-821X(83)90144-9

Noël, J., Godard, M., Oliot, E., Martinez, I., Williams, M., Boudier, F., Rodriguez, O., Chaduteau, C., Escario, S., Gouze, P., 2018. Evidence of polygenetic carbon trapping in the Oman Ophiolite: Petro-structural, geochemical, and carbon and oxygen isotope study of the Wadi Dima harzburgite-hosted carbonates (Wadi Tayin massif, Sultanate of Oman). Lithos 323, 218–237. https://doi.org/10.1016/J.LITHOS.2018.08.020

Oelkers, E.H., Berninger, U.N., Pérez-Fernàndez, A., Chmeleff, J., Mavromatis, V., 2018. The temporal evolution of magnesium isotope fractionation during hydromagnesite dissolution, precipitation, and at equilibrium. Geochim. Cosmochim. Acta 226, 36–49. https://doi.org/10.1016/j.gca.2017.11.004

Oskierski, H.C., Beinlich, A., Mavromatis, V., Altarawneh, M., Dlugogorski, B.Z., 2019. Mg isotope fractionation during continental weathering and low temperature carbonation of ultramafic rocks. Geochim. Cosmochim. Acta 262, 60–77. https://doi.org/10.1016/J.GCA.2019.07.019

Paukert, A.N., Matter, J.M., Kelemen, P.B., Shock, E.L., Havig, J.R., 2012. Reaction path

686 modeling of enhanced in situ CO2 mineralization for carbon sequestration in the peridotite
687 of the Samail Ophiolite, Sultanate of Oman. Chem. Geol. 330–331, 86–100.
688 https://doi.org/10.1016/j.chemgeo.2012.08.013

689 Pearce, C.R., Saldi, G.D., Schott, J., Oelkers, E.H., 2012. Isotopic fractionation during congruent
690 dissolution, precipitation and at equilibrium: Evidence from Mg isotopes. Geochim.
691 Cosmochim. Acta 92, 170–183. https://doi.org/10.1016/j.gca.2012.05.045

692 Pinilla, C., Blanchard, M., Balan, E., Natarajan, S.K., Vuilleumier, R., Mauri, F., 2015.
693 Equilibrium magnesium isotope fractionation between aqueous Mg2+ and carbonate
694 minerals: Insights from path integral molecular dynamics. Geochim. Cosmochim. Acta 163,
695 126–139. https://doi.org/10.1016/j.gca.2015.04.008

696 Power, I.M., Kenward, P.A., Dipple, G.M., Raudsepp, M., 2017. Room Temperature Magnesite
697 Precipitation. Cryst. Growth Des. 17, 5652–5659. https://doi.org/10.1021/acs.cgd.7b00311

698 Ryu, J.-S., Vigier, N., Decarreau, A., Lee, S.-W., Lee, K.-S., Song, H., Petit, S., 2016.
699 Experimental investigation of Mg isotope fractionation during mineral dissolution and clay
700 formation. Chem. Geol. 445, 135–145. https://doi.org/10.1016/j.chemgeo.2016.02.006

701 Saldi, G.D., Schott, J., Pokrovsky, O.S., Gautier, Q., Oelkers, E.H., 2012. An experimental study
702 of magnesite precipitation rates at neutral to alkaline conditions and 100–200 °C as a
703 function of pH, aqueous solution composition and chemical affinity. Geochim. Cosmochim.
704 Acta 83, 93–109. https://doi.org/10.1016/J.GCA.2011.12.005

705 Santiago Ramos, D.P., Coogan, L.A., Murphy, J.G., Higgins, J.A., 2020. Low-temperature
706 oceanic crust alteration and the isotopic budgets of potassium and magnesium in seawater.
707 Earth Planet. Sci. Lett. 541, 116290. https://doi.org/10.1016/j.epsl.2020.116290

708 Schauble, E.A., 2011. First-principles estimates of equilibrium magnesium isotope fractionation
709 in silicate, oxide, carbonate and hexaaquamagnesium(2+) crystals. Geochim. Cosmochim.
710 Acta 75, 844–869. https://doi.org/10.1016/J.GCA.2010.09.044

711 Schott, J., Mavromatis, V., Fujii, T., Pearce, C.R., Oelkers, E.H., 2016. The control of carbonate
712 mineral Mg isotope composition by aqueous speciation: Theoretical and experimental
713 modeling. Chem. Geol. 445, 120–134. https://doi.org/10.1016/j.chemgeo.2016.03.011

714 Shirokova, L.S., Mavromatis, V., Bundeleva, I.A., Pokrovsky, O.S., Bénézeth, P., Gérard, E.,
715 Pearce, C.R., Oelkers, E.H., 2013. Using Mg Isotopes to Trace Cyanobacterially Mediated
716 Magnesium Carbonate Precipitation in Alkaline Lakes. Aquat. Geochemistry 19, 1–24.
717 https://doi.org/10.1007/s10498-012-9174-3

718 Skarpelis, N., 2006. Lateritization processes of ultramafic rocks in Cretaceous times: The fossil
719 weathering crusts of mainland Greece. J. Geochemical Explor. 88, 325–328.
720 https://doi.org/10.1016/j.gexplo.2005.08.066

721 Snow, J.E., Dick, H.J.B., 1995. Pervasive magnesium loss by marine weathering of peridotite.
722 Geochim. Cosmochim. Acta 59, 4219–4235. https://doi.org/10.1016/0016-7037(95)00239-
723 V

724 Stanger, G., 1985. Silicified serpentinite in the Semail nappe of Oman. Lithos 18, 13–22.
725 https://doi.org/10.1016/0024-4937(85)90003-9

726 Streit, E., Kelemen, P.B., Eiler, J., 2012. Coexisting serpentine and quartz from carbonate-

727   bearing serpentinized peridotite in the Samail Ophiolite, Oman. Contrib. to Mineral. Petrol.
728   164, 821–837. https://doi.org/10.1007/s00410-012-0775-z

729   Su, B.-X., Teng, F.-Z., Hu, Y., Shi, R.-D., Zhou, M.-F., Zhu, B., Liu, F., Gong, X.-H., Huang,
730   Q.-S., Xiao, Y., Chen, C., He, Y.-S., 2015. Iron and magnesium isotope fractionation in
731   oceanic lithosphere and sub-arc mantle: Perspectives from ophiolites, Earth and Planetary
732   Science Letters. https://doi.org/10.1016/j.epsl.2015.08.020

733   Teng, F.-Z., 2017. Magnesium Isotope Geochemistry. Rev. Mineral. Geochemistry 82, 219–287.
734   https://doi.org/10.2138/rmg.2017.82.7

735   Teng, F.-Z., Li, W.-Y., Ke, S., Marty, B., Dauphas, N., Huang, S., Wu, F.-Y., Pourmand, A.,
736   2010. Magnesium isotopic composition of the Earth and chondrites. Geochim. Cosmochim.
737   Acta 74, 4150–4166. https://doi.org/10.1016/j.gca.2010.04.019

738   Teng, F.Z., Li, W.Y., Ke, S., Yang, W., Liu, S.A., Sedaghatpour, F., Wang, S.J., Huang, K.J.,
739   Hu, Y., Ling, M.X., Xiao, Y., Liu, X.M., Li, X.W., Gu, H.O., Sio, C.K., Wallace, D.A., Su,
740   B.X., Zhao, L., Chamberlin, J., Harrington, M., Brewer, A., 2015. Magnesium Isotopic
741   Compositions of International Geological Reference Materials. Geostand. Geoanalytical
742   Res. 39, 329–339. https://doi.org/10.1111/j.1751-908X.2014.00326.x

743   Tipper, E.T.T., Galy, A., Gaillardet, J., Bickle, M.J.J., Elderfield, H., Carder, E.A.A., 2006. The
744   magnesium isotope budget of the modern ocean: Constraints from riverine magnesium
745   isotope ratios. Earth Planet. Sci. Lett. 250, 241–253.
746   https://doi.org/10.1016/j.epsl.2006.07.037

747   Wang, W., Zhou, C., Liu, Y., Wu, Z., Huang, F., 2019. Equilibrium Mg isotope fractionation
748   among aqueous Mg2+, carbonates, brucite and lizardite: Insights from first-principles
749   molecular dynamics simulations. Geochim. Cosmochim. Acta 250, 117–129.
750   https://doi.org/10.1016/J.GCA.2019.01.042

751   Weyhenmeyer, C.E., Burns, S.J., Waber, H.N., Matter, A., 2002. Isotope study of moisture
752   sources , recharge areas , and groundwater flow paths within the eastern Batinah coastal
753   plain , Sultanate of Oman 38, 1–22. https://doi.org/10.1029/2000WR000149

754   Wimpenny, J., Colla, C.A., Yin, Q.-Z.Z., Rustad, J.R., Casey, W.H., 2014. Investigating the
755   behaviour of Mg isotopes during the formation of clay minerals. Geochim. Cosmochim.
756   Acta 128, 178–194. https://doi.org/10.1016/j.gca.2013.12.012

757   Wimpenny, J., Gíslason, S.R., James, R.H., Gannoun, A., Pogge Von Strandmann, P.A.E.,
758   Burton, K.W., 2010. The behaviour of Li and Mg isotopes during primary phase dissolution
759   and secondary mineral formation in basalt. Geochim. Cosmochim. Acta 74, 5259–5279.
760   https://doi.org/10.1016/j.gca.2010.06.028

761   Young, E.D., Galy, A., 2004. The Isotope Geochemistry and Cosmochemistry of Magnesium.
762   Rev. Mineral. Geochemistry 55, 197 LP – 230.

763
764